DOI: 10.13009/EUCASS2017-606

DOI: ADD DOINUMBER HERE

Large Eddy Simulation of trailing edge cutback film cooling: Impact of internal stiffening ribs on the adiabatic effectiveness

P. Aillaud[⋆†], *F. Duchaine*[⋆], *L. Y. M. Gicquel*[⋆], *C. Koupper*[⋆⋆] *and G. Staffelbach*[⋆]
[⋆]*Cerfacs*
42 avenue G. Coriolis 31 057 Toulouse Cedex 01 France
Email: aillaud@cerfacs.fr
[⋆⋆]*Safran Helicopter Engines*
SAFRAN Helicopter Engines 64510 Bordes, France
...
[†]Corresponding author

Abstract

This study deals with the Large Eddy Simulation (LES) of the film cooling technique at the trailing edge of a transonic vane equipped with a pressure side cutback. This configuration was studied experimentally at DLR within the framework of the European project AITEB-2. The cooling air is blown through a long slot and two rib arrays are placed inside the coolant channel to increase the stiffness of the thin trailing edge region. The simulation is first validated against global quantities such as the discharge coefficient and the blowing ratio as well as local quantities such as the isentropic Mach number and the adiabatic effectiveness. Then LES results are used to connect the flow dynamics to the adiabatic effectiveness observed in the cutback region. The interesting point is that the spatial period of the adiabatic effectiveness patterns, observed experimentally and numerically, is not the separation distance S in the spanwise direction between two consecutive ribs but is approximately $4S$. 3D flow visualizations highlight different physical phenomena present in the internal channel such as a separated flow at certain locations behind the diffuser array. It is shown that this separation is caused by a Coanda effect forcing the flow to follow the curvature of a profiled rib at some specific locations. This mechanism is used to explain the inhomogeneities observed in the spanwise direction for the adiabatic effectiveness. The separation regions behind the diffuser array cause an early attachment of the main flow to the cutback surface, detected with the skin friction lines, causing a rapid decrease of the the adiabatic effectiveness. This non-uniform film, generated by such a diffuser array, may affect the thermal behavior of the trailing edge.

1. Introduction

With current technologies, continuous improvement of gas turbine thermodynamic efficiency and increasing power demand unavoidably result in higher Turbine Entry Temperature (TET). It is well known that today the TET is above the maximum allowable blade metal temperature and keeps increasing. Development of advanced cooling systems is therefore a critical issue that needs to be addressed in the design phase to ensure that the turbine blades can durably sustain high temperature levels. Different techniques are used and can be divided into two main categories known as internal cooling, e.g. impinging jets and ribbed channel, and external cooling techniques, e.g. film cooling. The trailing edge region is one of the most critical part of the blade as it has to be thin to limit the aerodynamic losses. The state-of-the-art cooling systems for the trailing edge consist in blowing air, coming from internal cooling, through slots over a cutback on the pressure side as shown in Fig. 1. The effectiveness of the resulting film cooling is commonly measured with the adiabatic film effectiveness, η_{aw} defined in Eq. (1),

$$\eta_{aw} = \frac{T_{aw} - T_h}{T_h - T_c}, \tag{1}$$

where T_{aw} is the adiabatic wall temperature, T_h is the temperature of the hot gas and T_c is the temperature of the coolant. The adiabatic effectiveness usually varies from 1 at the slot exit to 0 far downstream where the coolant is mixed with

DOI: 10.13009/EUCASS2017-606

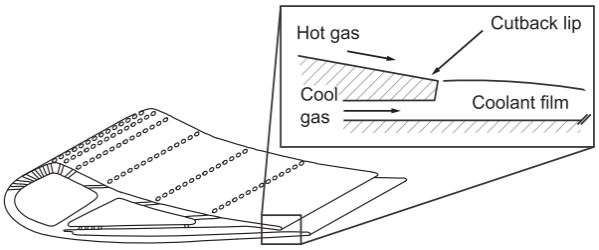

Figure 1: Trailing edge cutback for the generation of the film cooling on the pressure side, from Schneider et al. [1].

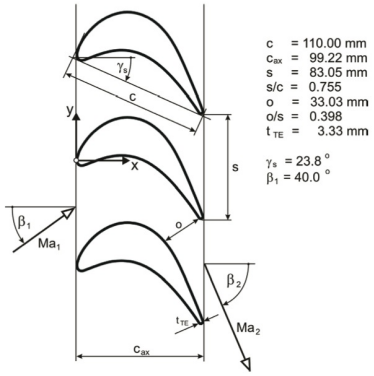

Figure 2: Cascade geometry and notations.

the mainstream. Past studies on simplified geometries have shown that the adiabatic effectiveness depends on various geometrical parameters [2,3], e.g. lip thickness to slot height ratio, as well as on flow parameters [4,5] such as the blowing ratio M defined as the ratio of the coolant momentum $(\rho U)_c$ to the mainstream momentum $(\rho U)_h$ where the subscripts c and h refer to the cold and hot gases. Trailing edge cutback flows also contain unsteadiness such as vortex shedding at the lip that can impact the adiabatic film effectiveness. This unsteady behavior was highlighted by Holloway et al. [6] in their numerical study using Unsteady Reynolds-Averaged Navier-Stokes (U-RANS) simulations. They show that steady RANS simulations were not able to capture the correct spatial distribution of the adiabatic effectiveness [7] that is mainly attributed to the vortex shedding phenomenon. Thereafter, many authors have studied experimentally and numerically with unsteady simulations, such as Large Eddy Simulation (LES) or Detached Eddy Simulation (DES), the interaction between the unsteady flow features and the effectiveness of the film cooling. [1,5,8–10] While flow features, such as the vortex shedding at the cutback lip, can impact the adiabatic film effectiveness, it was also shown that the internal cooling design can have a strong influence near the slot exit. [11,12]

Most of the above-mentioned studies deal with simplified configuration where the turbine blade is not present. Unsteady numerical simulations mentioned previously were performed for such a simplified configuration where the flow is considered incompressible. The main goal of this paper is to evaluate the LES capacity for the prediction of a realistic configuration of trailing edge film cooling installed in a linear cascade operating at compressible flow conditions close to real turbine vanes. The paper begins with the description of the retained experimental setup along with the description of the chosen operating point. Then, the numerical methods are described and the numerical results are compared to the experimental data in terms of flow dynamics and adiabatic film effectiveness. Finally, the LES results are used to relate the particular spatial distribution of the adiabatic effectiveness to the observed flow dynamics and organization.

2. Flow configuration

The experimental data used for this study come from a transonic linear cascade, shown in Fig. 2, installed at the DLR. [13,14] Three different trailing edge geometries with coolant ejection were tested within the framework of the European project AITEB-2. The configuration retained for this study is the pressure side cutback configuration shown in Fig. 3. It allows through the discharge of the internal coolant, the generation of a protective film on the pressure side of the trailing edge. One can note the presence of two rib arrays, colored in grey in Fig. 3, to increase the stiffness of the thin trailing edge region. A total of 36 operating points, summarized in Table 1, have been studied during the

DOI: 10.13009/EUCASS2017-606

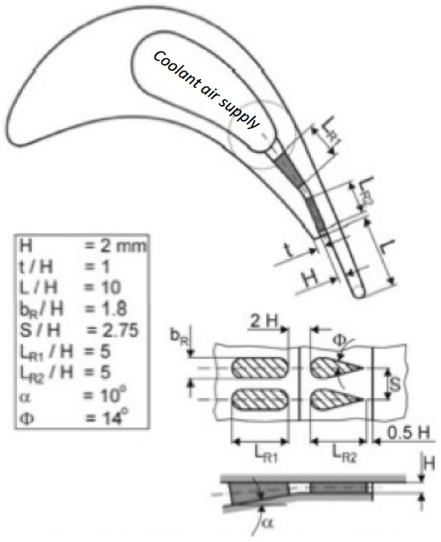

Figure 3: Trailing edge cooling geometries.

experimental test campaign. Each operating point is defined by an exit isentropic Mach number $Ma_{2,is}$ and a coolant mass flow ratio c_m expressed as the ratio of the coolant mass flow per blade to the sum of the main mass flow through a blade passage (throat area) and the coolant mass flow. The operating point chosen for this study is $Ma_{2,is} = 1.1$ and $c_m = 2\%$ close to the operating conditions found in real engine.

Table 1: Operating points of the experimental test campaign.

$\mathbf{Ma_{2,is}}$					
0.7	0.8	0.9	1.0	1.1	1.2
$\mathbf{c_m}[\%]$					
0	0.25	0.5	1	1.5	2

3. Numerics

3.1 Solver

The parallel LES solver AVBP[15] developed by CERFACS and IFPEN is used to solve the filtered compressible Navier-Stokes equations on unstructured meshes. A finite element two-step time-explicit Taylor Galerkin scheme (TTG4A)[16] is used for the discretization of the convective terms based on a cell-vertex formulation. The scheme is fourth-order in time and third-order in space while ensuring low dispersion and diffusion properties which is in agreement with the requirements of LES applications.[17] A second order Galerkin scheme is used for diffusion terms.[18] Such numerics are especially designed for LES on hybrid meshes and have been extensively validated for a wide range of turbulent flow applications.[19–23] The explicit temporal integration is the major drawback of this strategy because the timestep is limited, for stability reasons, by the acoustic Courant Friedrichs Lewy number (CFL = 0.7 for this study leading to $\Delta t \approx 0.16\mu$s). The unresolved Sub-Grid Scale (SGS) stress tensor is modelled using the Boussinesq assumption[24] and the SGS viscosity is computed with the Wall Adapting Local Eddy-viscosity (WALE) model that is well suited for wall-resolved LES as it recovers the proper y^3 near-wall scaling of the eddy viscosity.[25] The SGS heat fluxes are modelled using the classical gradient-diffusion hypothesis[24] that relates the SGS heat flux to the filtered temperature gradient using a SGS thermal conductivity. This approach postulates a direct analogy between the momentum and heat transfer through the SGS turbulent Prandtl number ($Pr_{SGS} = \mu_{SGS}\ C_p(T)/\lambda_{SGS}$), here fixed at $Pr_{SGS} = 0.5$.

DOI: 10.13009/EUCASS2017-606

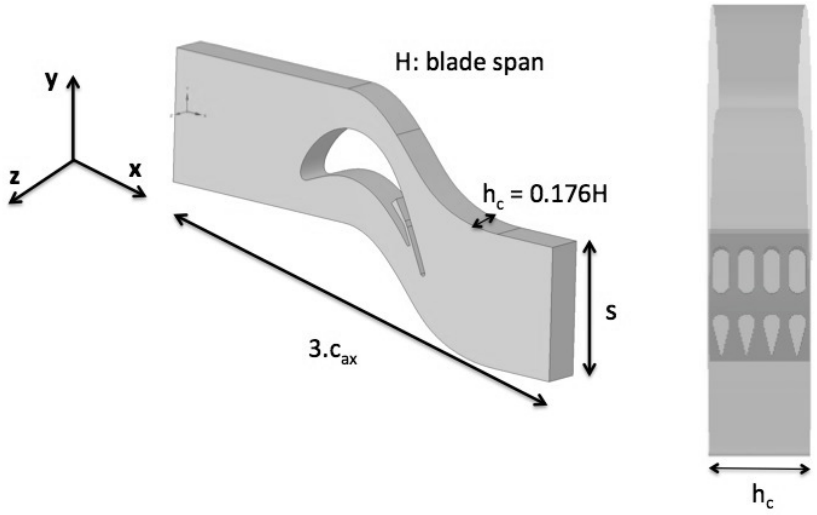

Figure 4: Computational domain.

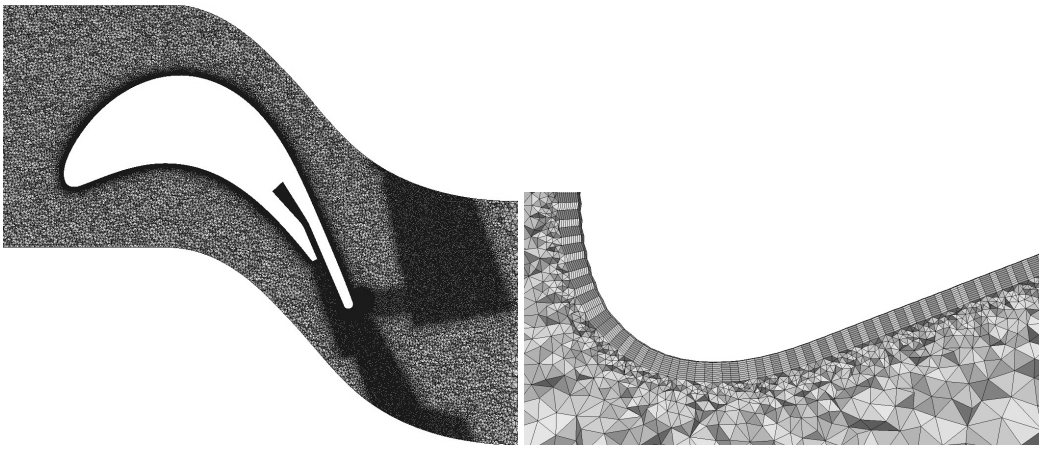

(a) (b)

Figure 5: 2D Z-normal cut of the mesh showing a global view with the specific refinement regions (a) and the prism layers at the wall on the blade (b).

3.2 Computational domain & grid

The computational domain used for this study is presented in Fig. 4. It contains only the central passage of the linear cascade assuming periodic boundary conditions in the pitchwise direction. To limit the computational cost, periodicity is also assumed is the spanwise direction and only 4 cooling passages are simulated. The inlet of the domain is located at one axial chord length, c_{ax}, upstream the blade leading edge while the outlet is placed at a distance c_{ax} downstream of the blade trailing edge. The total axial length of the domain is thus $3c_{ax}$. A hybrid strategy is chosen for the mesh generation with tetrahedral elements inside the computational domain and ten prism layers at the wall. Specific refinements are located in regions of interest, i.e. the trailing edge region, the wake and the coolant-mainstream interaction region. These refinement regions are shown in Fig. 5 along with the prism layers at the walls. The mesh between the ribs is also shown in Fig. 6. The mesh is composed of a total of 24 millions grid cells.

3.3 Boundary conditions

Total pressure $P_{t,1}$ and total temperature $T_{t,1}$ as well as the flow angle are imposed using the NSCBC formalism[26] at the inlet as shown in Fig. 7. At the outlet the static pressure, $P_{s,2}$, is relaxed towards the mean reference pressure using the

DOI: 10.13009/EUCASS2017-606

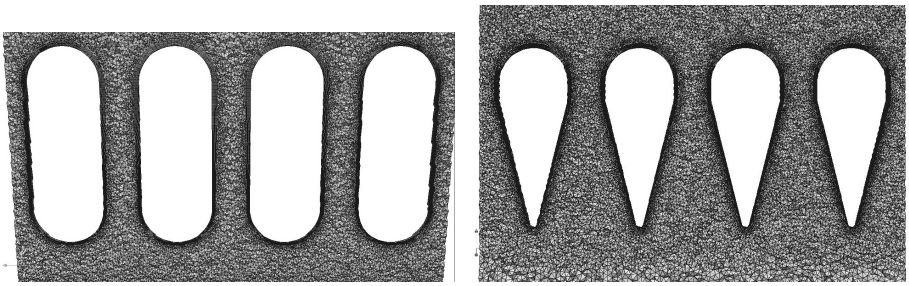

(a) (b)

Figure 6: 2D cut of the mesh showing the first (a) and second (b) row of ribs.

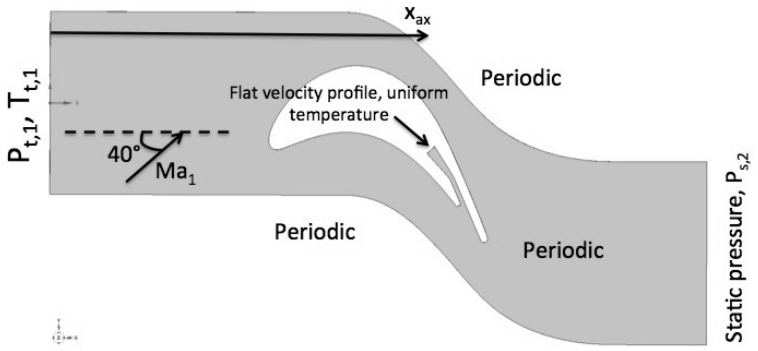

Figure 7: Boundary conditions.

NSCBC formalism.[26] $P_{t,1}$ and $P_{s,2}$ are set to get the correct isentropic Mach number at the exit of the domain $Ma_{2,is}$ defined in Eq. (2),

$$Ma_{2,is} = \sqrt{\frac{2}{\gamma - 1}\left[\left(\frac{P_{t,1}}{P_{s,2}}\right)^{\frac{\gamma-1}{\gamma}} - 1\right]}, \tag{2}$$

where γ is the specific heat ratio of air. $T_{t,1}$ is the total temperature measured at the inlet during the experiment. For the coolant, the flow is relaxed towards a mean reference state[26] using a flat velocity profile, a constant mass flow rate and a constant temperature $T_{c,i}$ set to the experimental value, i.e. $T_{c,i} = 263.15K$. The mass flow rate is calculated from the inlet flow conditions to get the correct c_m. The ribs and the blade are treated as adiabatic no slip walls. Note also that air is used for both the coolant and the fluid in the mainstream.

4. Results and Discussions

This section provides a validation and analysis of the LES results. The mean flow predictions are presented first followed by the adiabatic film effectiveness results. Finally, these two parts are linked to explain the particular spatial distribution of the adiabatic effectiveness on the cutback surface. The statistics presented hereafter are accumulated over 4 convective times with one convective time defined as $t_{conv} = c/U_{bulk,1}$ where $U_{bulk,1}$ is the bulk velocity at the inlet of the computational domain. Whenever applicable, quantities of interest are also averaged in the homogeneous spanwise direction. The computational cost to do one convective time is about 3000 CPU hours on 480 cores of the Bull machine OCCIGEN of GENCI installed at CINES. All the experimental results reported in this section are provided by SAFRAN Helicopter Engines.

4.1 Validation of the flow dynamics

A wall resolved approach is targeted for this study and the normalized near wall distance y^+ is presented in Fig. 8. With this grid, the near wall resolution ranges from $y^+ = 3$ to $y^+ = 30$. On the internal ribs, the y^+ values, not shown in Fig. 8, range from $y^+ = 2$ to $y^+ = 20$. These values are relatively high to consider that the first computational node is inside the viscous sublayer everywhere on the walls. This simulation can not be strictly called wall resolved but the

DOI: 10.13009/EUCASS2017-606

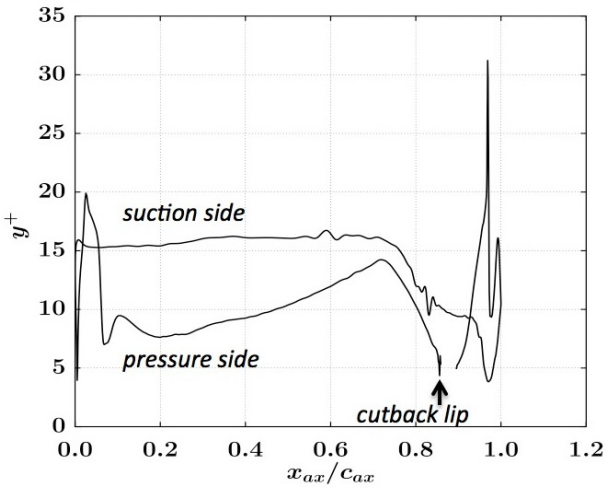

Figure 8: y^+ on the external skin of the blade as a function of the non dimensional axial distance x_{ax}/c_{ax}.

comparisons to the experiments and the analysis made in this study tends to show that the performance of the trailing edge film cooling is not mainly driven by the flow close to the wall. As a consequence, this near wall resolution is found to be adequate for the problem investigated here.

Some global quantities such as the blowing ratio, M, or the discharge coefficient, c_d are measured experimentally and can be used to assess the validity of the simulation. The blowing ratio, defined in Eq. (3), is the ratio of the coolant mass flux to the local isentropic main mass flux,

$$M = \frac{(\rho U)_{c,o}}{(\rho U)_1}, \tag{3}$$

where ρ is the local fluid density and U is the local normal velocity. Quantities indexed c, o are related to the coolant flow and are measured at the slot exit plane while quantities indexed 1 are related to the mainstream. The discharge coefficient, defined in Eq. (4) is the ratio of the coolant mass flow measured experimentally or numerically to the ideal mass flow for isentropic conditions from the coolant injection to the slot exit,

$$c_d = \frac{\dot{m}_c}{A_c P_{t,c,i}\left(\frac{P_{t,c,i}}{P_c}\right)^{\frac{-(\gamma+1)}{2\gamma}} \sqrt{\frac{2\gamma}{(\gamma-1)\cdot R\cdot T_{t,c,i}}\left[\left(\frac{P_{t,c,i}}{P_c}\right)^{\frac{\gamma-1}{\gamma}} - 1\right]}}, \tag{4}$$

where $\dot{m}_c$ is the coolant mass flow rate, A_c is the slot exit plane surface, $P_{t,c,i}$ and $T_{t,c,i}$ are the total pressure and the total temperature at the inlet of the coolant channel, P_c is the static pressure at the slot exit plane and R is the specific gas constant.

Results for M and c_d are presented in Fig. 9 as a function of the coolant mass flow ratio. The results obtained from the simulation are indicated by filled symbols. As expected the blowing ratio is proportional to the coolant mass flow ratio and the prediction is in agreement with the experimental tendency. The discharge coefficient is relatively low, around $c_d = 0.3$, indicating a high level of pressure loss due the presence of the ribs. One can note that the prediction for c_d is quite good despite the relatively high y^+ values found on the ribs that are treated as no-slip walls. This probably means that the singular loss term is dominant in the total pressure drop and well captured by the present simulation.

The local validation for the dynamics is achieved by looking at the pressure fields around the blade. Indeed, assuming that the pressure gradient in the direction normal to the wall is negligible within the boundary layer, the static pressure distribution on the blade is a good representation of the flow field around the blade outside of the boundary layer. The pressure fields are compared in terms of isentropic Mach number Ma_{is} as defined in Eq. (2) where $P_{s,2}$ is replaced by the static pressure on the blade $P_{s,b}$. Experimentally, two configurations presented in Fig. 10, have been studied for which $P_{s,b}$ is measured using static pressure taps that are represented as dots. The first configuration is a solid blade without any ejection system and have pressure taps installed all along the blade skin (see Fig. 10a). Configuration 2 is cooled and equipped with a pressure side cutback. It has pressure taps installed only on a limited part of the blade skin (see Fig. 10b). Because of this, the LES data are first compared to the solid blade, i.e. non cooled blade, in Fig. 11 to be able to compare the results all along the blade skin. On the suction side, the flow is strongly accelerated and becomes supersonic at $x_{ax}/c_{ax} \approx 0.65$. Then, the flow remains supersonic and no shock

DOI: 10.13009/EUCASS2017-606

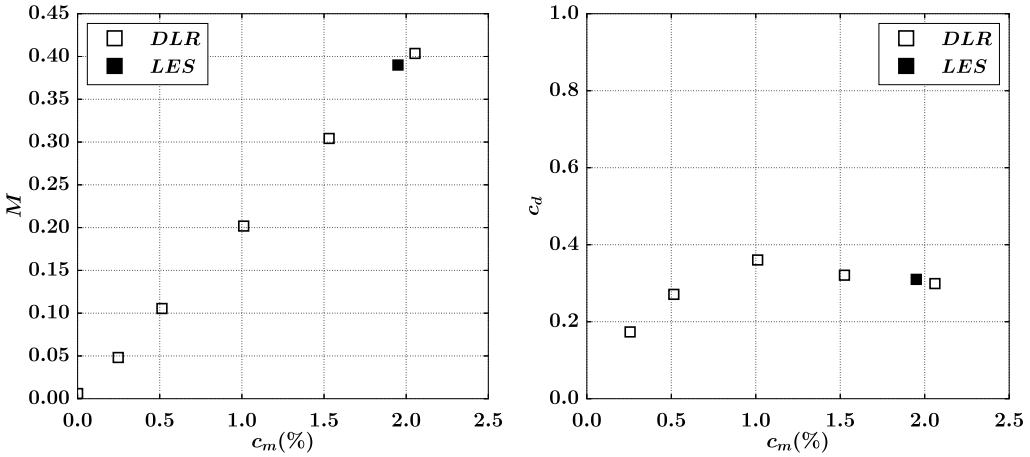

(a) (b)

Figure 9: Blowing ratio M (a) and discharge coefficient c_d (b) as a function of the coolant mass flow ratio. (■): LES results, (□): experimental results.

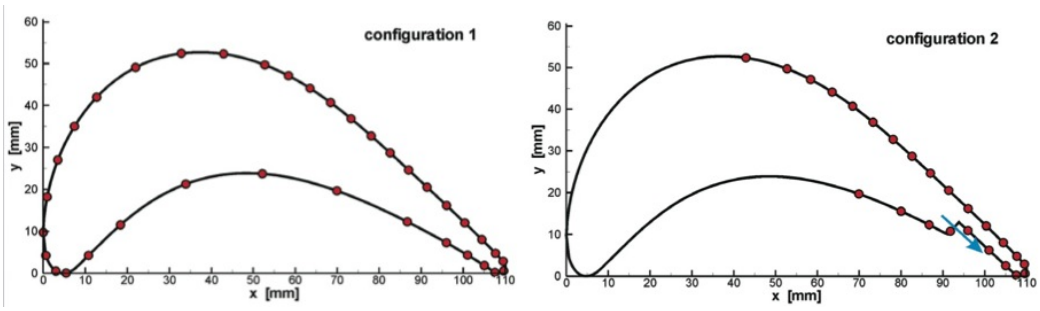

(a) (b)

Figure 10: Experimental configurations used for the measurements of the isentropic Mach number around the blade. Solid blade (a) and blade equipped with the pressure side cutback ejection system (b).

DOI: 10.13009/EUCASS2017-606

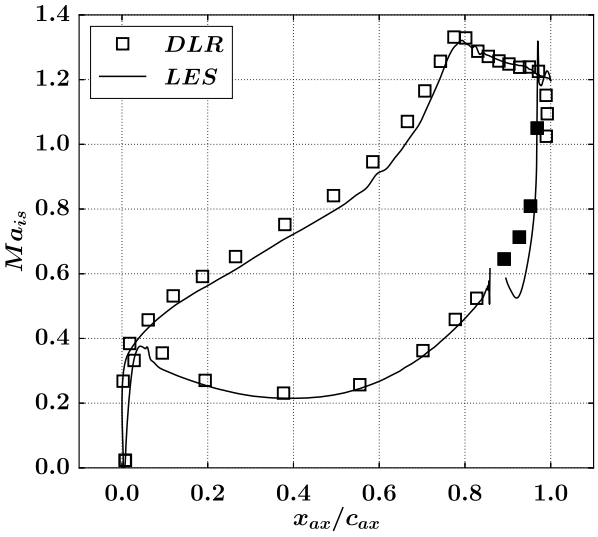

Figure 11: Isentropic mach number, Ma_{is}, on the external skin of the blade as a function of the non-dimensional axial distance x_{ax}/c_{ax}. (−): LES. (□): Experimental data obtained for the solid blade configuration (configuration 1). (■): Pressure taps located at the axial position of the pressure side cutback that is present only for LES results.

appears on the blade. On the pressure side, the flow accelerates first due to the presence of the stagnation region and a small convex region inducing a favorable pressure gradient in the streamwise direction. Then, the flow is exposed to an adverse pressure gradient, due to the concave curvature, that causes its deceleration shortly downstream of the stagnation point. A good agreement is found between the experimental and LES results indicating a good prediction of the flow field around the blade with LES. Note that the filled symbols should not be considered as they are located in the region of the pressure side cutback that is present in LES but not in the experimental results for the solid blade configuration. Figure 12 shows the experimental isentropic mach number for the pressure side cutback geometry, i.e. cooled configuration. Overall, there is a good agreement between the experimental and LES results including in the cutback region. The largest discrepancies are located in a small region around the trailing edge. The flow is separating at the cutback lip and reattaches further downstream to the cutback surface. The reattachment point corresponding to the local minimum on the pressure side at $x_{ax}/c_{ax} \approx 0.95$ for the LES results can be identified in Fig. 12. Note also that there is a small region where the flow is supersonic in the cutback region. Finally, the Schlieren picture is compared to the density gradient obtained in the simulation in Fig. 13. The numerical prediction provides a good localization of the normal shock just downstream of the trailing edge that marks the end of the supersonic region. A lambda shaped shock is also observed in both pictures, just upstream of the trailing edge on the suction side, possibly linked to a flow separation due to the adverse pressure gradient in this region.

The flow obtained with the LES has been validated in terms of mean global quantities, mean local quantities as well as view of the main flow features. The objective is now to compare and analyze the results in terms of film cooling performance.

4.2 Validation of the adiabatic effectiveness

The basic idea behind the use of the pressure side cutback is to generate a protective film to limit the heat transfer between the hot mainstream and the blade in the thin trailing edge region. One way to assess the performance of such a system is to look at the adiabatic effectiveness that in a linear cascade can be defined as in Eq. (5),

$$\eta_{aw} = \frac{T_{aw} - T_r}{T_{c,o} - T_r}, \tag{5}$$

where T_{aw} is the wall temperature under adiabatic condition, obtained with a coolant injected at $T_{c,i} < T_1$ with T_1 the static temperature at the inlet of the domain. T_r is the wall temperature under adiabatic condition, obtained with a coolant injected at $T_{c,i} = T_1$. $T_{c,o}$ is the coolant temperature measured at the slot exit. The adiabatic effectiveness computed on the cutback region is presented in the coordinate system shown in Fig. 14.

The experimental and LES results obtained for η_{aw} are shown in Fig. 15a. One can note the presence of a quasi-periodic pattern in the experimental results with 2 regions of low values of η_{aw} located at $z/S \approx 2$ and $z/S \approx -2$. This

DOI: 10.13009/EUCASS2017-606

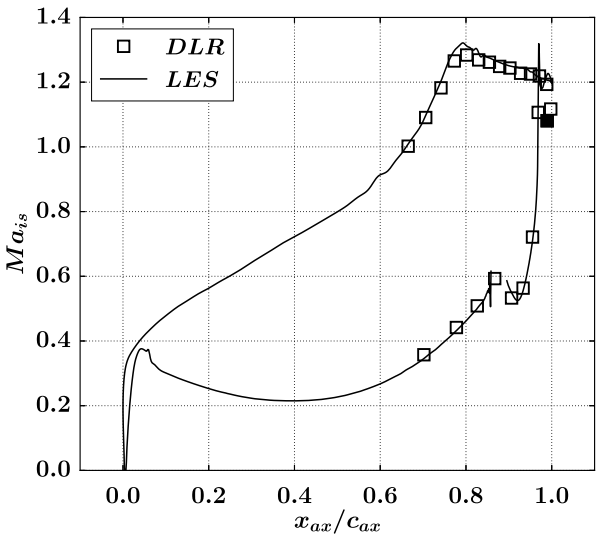

Figure 12: Isentropic mach number, Ma_{is},on the external skin of the blade as a function of the non-dimensional axial distance x_{ax}/c_{ax} for the pressure side cutback geometry, i.e. configuration 2. (■): Pressure tap located at the trailing edge.

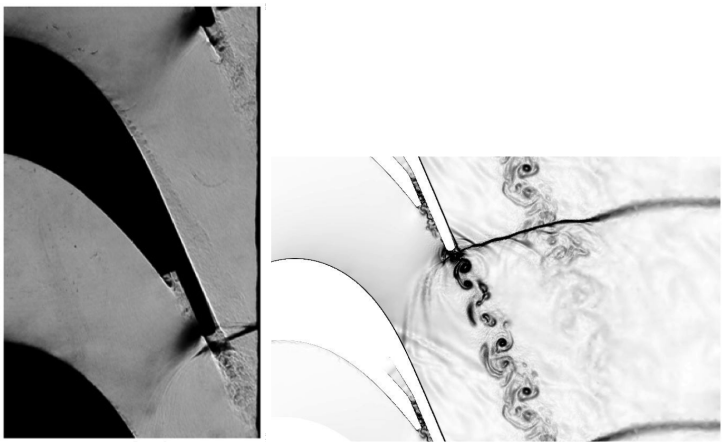

(a) (b)

Figure 13: 2D Z-normal cut representing the density gradient. Experimental Schlieren photography (a) and instantaneous LES results, $\|\vec{\nabla}\rho\|/\rho$ (b).

DOI: 10.13009/EUCASS2017-606

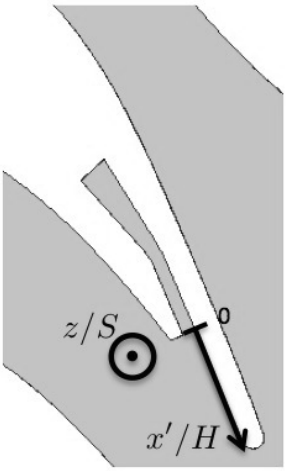

Figure 14: Coordinate system for the observation of the adiabatic effectiveness η_{aw}.

observation supports the use of a periodic computational domain in the spanwise z direction. To help the reader for the localization of the different patterns regarding the position of the ribs, Fig. 15b presents the ribs along with the z/S axis. At $z/S = 0$, a region of relatively high values of η_{aw} is present in the experiment and in the LES. The region extends along the x' direction. The spike, represented by the isoline $\eta_{aw} = 0.7$ is more pronounced in the LES than in the experiment reaching respectively $x'/H \approx 7$ and $x'/H \approx 5$. The region of high η_{aw} values is surrounded by two regions of low η_{aw} values located near $z/S \approx \pm 2$. This kind of periodic pattern was already observed experimentally by Martini and Schulz [11] for a subsonic academic configuration with a double in-line rib array in the coolant channel. They suspect a coalescence of several jets due to the Coanda effect explaining the occurrence of such characteristic patterns. They showed that the patterns depend on the blowing ratio with sometimes two or three jets coalescing. For low blowing ratio, i.e. $M = 0.5$, they state that the coalescence of several jets is an unsteady phenomenon and that the state of separated jets is unstable and only exists for a few seconds. The geometry and flow conditions used in the present study are different from the one used by Martini and Schulz.[11] Here the second row of ribs acts as a diffuser and the coolant channel is in a transonic linear cascade. A more qualitative comparison between experimental and numerical results is presented in Fig. 16 showing the adiabatic film effectiveness at $z/S = -1$ and $z/S = 1$ as well as the spanwise average of η_{aw}. A fairly good agreement is found, but discrepancies are observed near the slot exit where η_{aw} is always higher in the experiment compared to the numerical results. One explanation for the observed differences could be the uncertainty in the location of the measurement points in the experimental data.

In the next part, the LES results are used to gain insight in the flow dynamics for the present configuration and to explain the characteristic patterns observed for η_{aw} based on the previous observation of Martini and Schulz.[11]

4.3 Link between the flow dynamics and the adiabatic effectiveness

LES gives access to the full 3D instantaneous flow field allowing to gain insight in the flow organization inside the coolant channel. To visualize the organization of the flow a tracer is injected at the inlet of the coolant channel. The evolution in time of the concentration of the tracer is presented in Fig. 17. Two ribs are identified as *Rib* 0 and *Rib* 2 in Fig. 17a and correspond respectively to the ribs located at $z/S = 0$ and $z/S = 2$ in Fig. 15b. These are respectively the location of high and low adiabatic effectiveness on the pressure side cutback surface. For time t_0, the tracer has reached the first rib row. The reduction of the cross section forces the flow to accelerate and generates 4 jets which start to interact with the diffuser array. At time t_1, the Coanda effect is clearly seen for the flow passing around *Rib* 0. The jets on both sides follow the convex surface curvature and at time t_2 the two jets are attached to *Rib* 0. The merging of the 2 jets generates low pressure regions for ribs on both sides of *Rib* 0 and finally, at time t_3, all the jets coalesce around *Rib* 0. As a consequence a low speed zone is observed in the wake of *Rib* 2 where the adiabatic film effectiveness is poor. To complement these instantaneous visualizations, the mean flow organization is shown in Fig. 18. The mean streamlines highlight the presence of a low speed zone behind *Rib* 2 as a consequence of the coalescence of the jets. Looking at the friction lines behind *Rib* 2 at $z/S = 2$, this low speed area is in fact a recirculation zone with the mean flow going against the main flow direction, i.e. in the positive x' direction. The friction lines are also found to converge to the location $z/S = 0$, i.e. behind *Rib* 0, in between the two recirculation zones. Downstream the recirculation, the

DOI: 10.13009/EUCASS2017-606

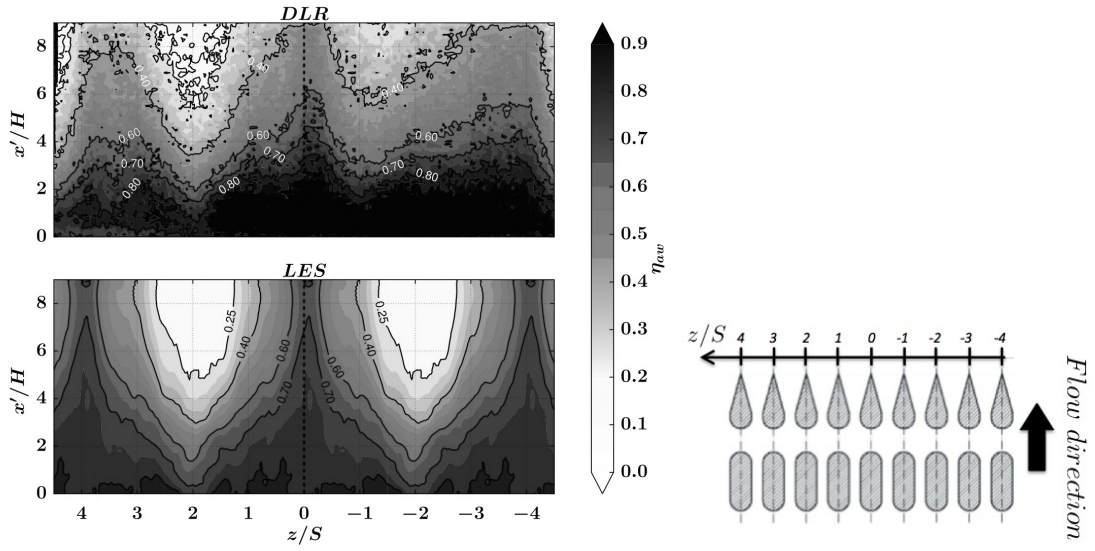

Figure 15: Adiabatic effectiveness η_{aw} in the $(x'/H, z/S)$ plane (a) and localization of the ribs as a function of z/S (b). The LES computation is periodic in the z direction and the computational domain, including 4 passages, corresponds to $-1.5 \leq z/S \leq 2.5$.

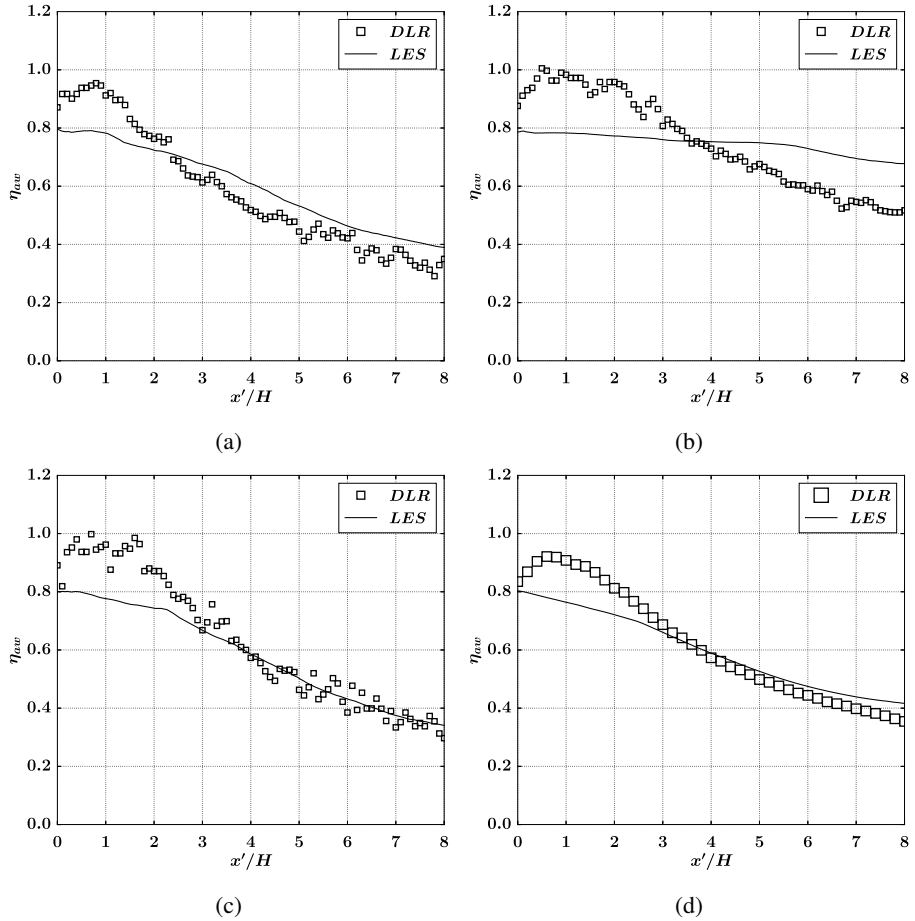

Figure 16: Adiabatic effectiveness η_{aw} as a function of x'/H at $z/S = -1$ (a), $Z/S = 0$ (b) and $z/S = 1$ (c). Adiabatic effectiveness η_{aw} averaged in space in the spanwise direction z/S (d).

DOI: 10.13009/EUCASS2017-606

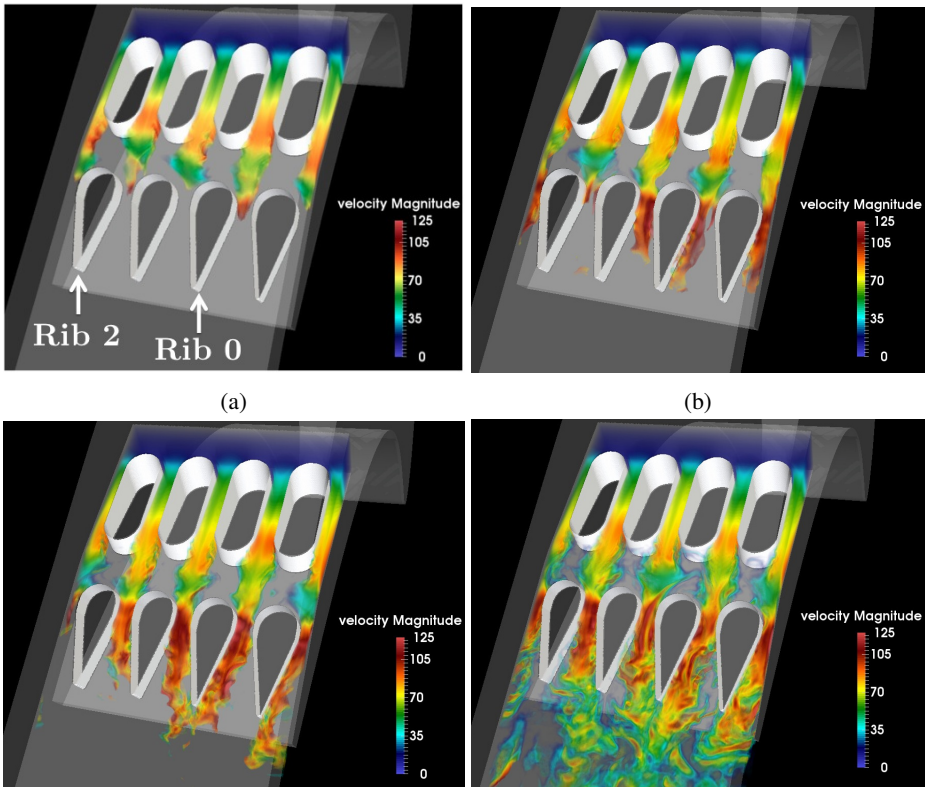

Figure 17: Volume rendering of the instantaneous concentration of a tracer colored by the velocity magnitude U_{mag} at time t_0 (a), t_1 (b), t_2 (c), t_3 (d) with $t_3 > t_2 > t_1 > t_0$. The opacity goes linearly from 0 for $U_{mag} = 0\ m/s$, to 1 for $U_{mag} = 125\ m/s$.

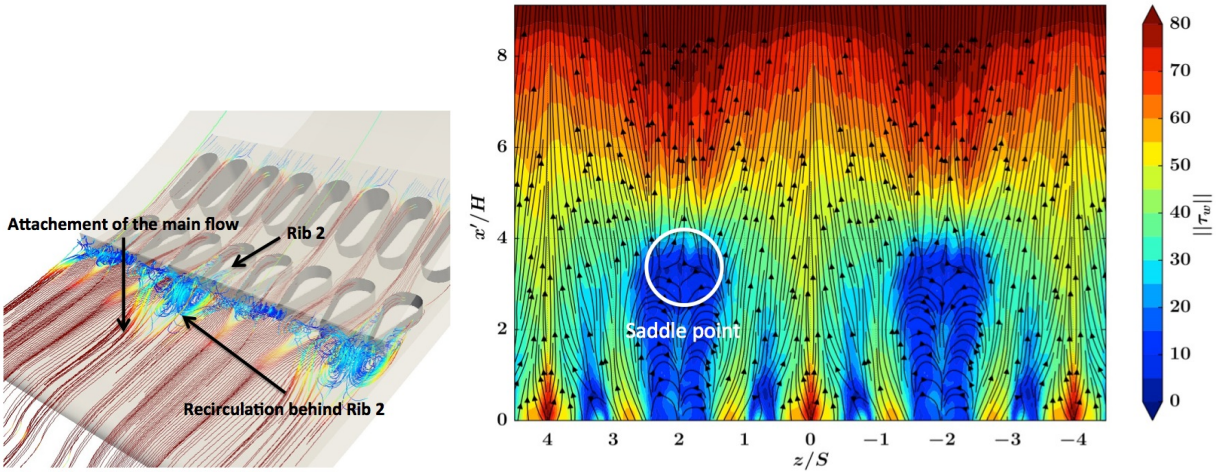

Figure 18: Mean flow organization with the mean streamlines colored by the velocity magnitude (blue for low velocity and red for high velocity) (a) and the mean friction lines along with the magnitude of the wall shear stress τ_w on the cutback surface (b).

DOI: 10.13009/EUCASS2017-606

flow coming from the hot mainstream attaches to the cutback surface at the saddle point identified in Fig. 18b causing a rapid decrease of the adiabatic film effectiveness.

5. Conclusions

In this work, a LES of a trailing edge cutback geometry operated in a transonic linear cascade has been carried out. The configuration is equipped with internal stiffening ribs that are commonly found in real industrial applications. The LES results have been validated against experiments in terms of blowing ratio, discharge coefficient and isentropic Mach number distribution around the blade. It has been shown that the flow dynamics is correctly captured by the simulation despite a near wall resolution that is deemed slightly too coarse compared to the usual recommendations for wall resolved LES. Spatial distribution of the adiabatic film effectiveness has also been compared to the experimental results. A relatively good agreement is found although the spatial periodicity of the adiabatic effectiveness that is enforced in the simulation is not so clear in the experimental results. However and thanks to the present unsteady predictions, these periodic patterns of the adiabatic effectiveness, that were previously observed by Martini and Schulz [11] for a different configuration and operating conditions, can clearly be linked to the flow dynamics. The main conclusion is that a Coanda effect takes place in the diffuser array causing a coalescence of the jets. This effect is the main cause of the spanwise inhomogeneities of the adiabatic effectiveness because of an early attachment of the mainstream to the cutback surface. This unintended consequence of the presence of the stiffening ribs should be considered during the design of such a system as the non-uniform protection can potentially affect the thermal behavior of the trailing edge.

Aknowledgements

The authors acknowledge CINES of GENCI for giving access to HPC ressources under the allocation 2017-x20172a6074. The authors are grateful to SAFRAN Helicopter Engines for funding this work and the AITEB-2 consortium funded by Europe, FP6, contract number “AST4-CT-2005-516113”, for providing the experimental results. Some of the post-processing was performed using Antares [28] and the Antares team is gratefully acknowledged for providing the library and support.

References

[1] H. Schneider, D. A. Von Terzi, H-J. Bauer, and W. Rodi. Coherent structures in trailing-edge cooling and the challenge for turbulent heat transfer modelling. *International Journal of Heat and Fluid Flow*, 51:110–119, 2015.

[2] M. E. Taslim. Experimental investigation of film cooling effectiveness for slots of various exit geometries. *Journal of Thermophysics and Heat Transfer*, 6(2):302–307, 1992.

[3] R. Becchi, B. Facchini, A. Picchi, L. Tarchi, D. Coutandin, and S. Zecchi. Film cooling adiabatic effectiveness measurements of pressure side trailing edge cooling configurations. *Propulsion and Power Research*, 4(4):190–201, 2015.

[4] G. Bittlinger, A. Schulz, and S. Wittig. Film cooling effectiveness and heat transfer coefficients for slot injection at high blowing ratios. In *International Gas Turbine and Aeroengine Congress and Exposition*, 1994.

[5] Z. Yang and H. Hu. An experimental investigation on the trailing edge cooling of turbine blades. *Propulsion and Power Research*, 1(1):36–47, 2012.

[6] D. S. Holloway, J. H. Leylek, and F. A. Buck. Pressure-side bleed film cooling: Part II - Unsteady framework for experimental and computational results. *ASME Turbo Expo*, 2002.

[7] D. S. Holloway, J. H. Leylek, and F. A. Buck. Pressure-side bleed film cooling: Part I - Steady framework for experimental and computational results. In *ASME Turbo Expo*, 2002.

[8] G. Medic and P. A. Durbin. Unsteady Effects on Trailing Edge Cooling. *Journal of Heat Transfer*, 127(4): 388–392, 2005.

[9] J. Joo and P. Durbin. Simulation of turbine blade trailing edge cooling. *Journal of Fluids Engineering*, 131(2), 2009.

DOI: 10.13009/EUCASS2017-606

[10] G. Barigozzi, A. Armellini, C. Mucignat, and L. Casarsa. Experimental investigation of the effects of blowing conditions and Mach number on the unsteady behavior of coolant ejection through a trailing edge cutback. *International Journal of Heat and Fluid Flow*, 37:37–50, 2012.

[11] P. Martini and A. Schulz. Experimental and Numerical Investigation of Trailing Edge Film Cooling by Circular Coolant Wall Jets Ejected From a Slot With Internal Rib Arrays. *Journal of Turbomachinery*, 126:229–236, 2004.

[12] P. Martini, A. Schulz, and H-J. Bauer. Film Cooling Effectiveness and Heat Transfer on the Trailing Edge Cutback of Gas Turbine Airfoils With Various Internal Cooling Designs. *Journal of Turbomachinery*, 128:196, 2006.

[13] A. Dannhauer. Investigation of Trailing Edge Cooling Concepts in a High Pressure Turbine Cascade: Analysis of the Adiabatic Film Cooling Effectiveness. In *ASME Turbo Expo*, pages 301–310. ASME, 2009. ISBN 978-0-7918-4884-5. doi: 10.1115/GT2009-59343.

[14] H-J. Rehder. Investigation of Trailing Edge Cooling Concepts in a High Pressure Turbine Cascade: Aerodynamic Experiments and Loss Analysis. *Journal of Turbomachinery*, 134(5):051029, 2012. doi: 10.1115/1.4004748.

[15] T. Schønfeld and M. Rudgyard. Steady and unsteady flows simulations using the hybrid flow solver avbp. *AIAA Journal* , 37(11):1378–1385, 1999.

[16] L. Quartapelle and V. Selmin. High-order Taylor-Galerkin methods for non-linear multidimensional problems., 1993.

[17] N. Lamarque. *Schémas numériques et conditions limites pour la simulation aux grandes échelles de la combustion diphasique dans les foyers d'hélicoptère*. Phd thesis, INP Toulouse, 2007.

[18] J. Donea and A. Huerta. *Finite Element Methods for Flow Problems*. John Wiley & Sons Inc, New York, 2003.

[19] S. Mendez and F. Nicoud. Large-eddy simulation of a bi-periodic turbulent flow with effusion. *Journal of Fluid Mechanics*, 598:27–65, 2008. doi: 10.1017/S0022112007009664.

[20] A. Dauptain, B. Cuenot, and L. Y. M. Gicquel. Large Eddy Simulation of Stable Supersonic Jet Impinging on Flat Plate. *AIAA Journal*, 48(10):2325–2338, 2010.

[21] F. Duchaine, N. Maheu, V. Moureau, G. Balarac, and S. Moreau. Large-Eddy Simulation and conjugate heat transfer around a low-Mach turbine blade. *Journal of Turbomachinery*, 136(5):051015, 2013. doi: 10.1115/1.4025165.

[22] L. Y. M. Gicquel, G. Staffelbach, and T. Poinsot. Large eddy simulations of gaseous flames in gas turbine combustion chambers. *Prog. Energy Comb. Sci.* , 38(6):782 – 817, 2012.

[23] F. Shum-kivan, F. Duchaine, and L. Gicquel. Large-eddy simulation and conjugate heat transfer in a round impinging jet. In *ASME Turbo Expo*, 2014.

[24] S. B. Pope. *Turbulent flows*. Cambridge University Press, 2000.

[25] F. Nicoud and F. Ducros. Subgrid-scale stress modelling based on the square of the velocity gradient. *Flow, Turb. and Combustion* , 62(3):183–200, 1999.

[26] T. Poinsot and S. Lele. Boundary conditions for direct simulations of compressible viscous flows. *J. Comput. Phys.* , 101(1):104–129, 1992. doi: 10.1016/0021-9991(92)90046-2.

[27] H. Chung, H-S. Sohn, J. S. Park, K. M. Kim, and H. H. Cho. Thermo-structural analysis of cracks on gas turbine vane segment having multiple airfoils. *Energy*, 118:1275–1285, 2017. doi: 10.1016/j.energy.2016.11.005.

[28] Antares: pre, post and co-processing library. URL `http://cerfacs.fr/antares/`.